Carbon 165 (2020) 296–305

Contents lists available at ScienceDirect

Carbon

journal homepage: www.elsevier.com/locate/carbon

Facile and cost-effective manipulation of hierarchical carbon nanosheets for pseudocapacitive lithium/potassium storage

Tingyue Peng , Zhonghao Tan , Mengdi Zhang , Linqing Li , Yixian Wang , Lu Guan , Xiaojie Tan , Lei Pan , Haiqiu Fang , Mingbo Wu *

State Key Laboratory of Heavy Oil Processing, College of New Energy, College of Chemical Engineering, China University of Petroleum (East China), Qingdao, 266580, PR China

ARTICLE INFO

Article history:
Received 10 February 2020
Received in revised form
11 April 2020
Accepted 14 April 2020
Available online 23 April 2020

ABSTRACT

The rising demand for high-performance energy storage devices calls for cost-effective electrode materials with large working potential windows, high specific capacities, and rapid rate capability. Herein, we propose a facile molten-salt-mediated production of ultrathin carbon nanosheets with tunable nitrogen doping using low-cost precursors including asphalt and melamine. The as-obtained nitrogen doped slim carbon nanosheets (NSCN) constructed through this easy and effective *in-situ* method offer both high specific capacity and excellent cycling stability. Specifically, a specific capacity of 848 mAh g^{-1} after 800 cycles at 1 A g^{-1} and 214 mAh g^{-1} after 1500 cycles at 1 A g^{-1} were achieved for lithium and potassium storage, respectively. The excellent electrochemical performances benefit from the synergistic effect of structural merits including ultra-thin nanosheet, nitrogen doping, high disorder degree and large specific surface area. Meanwhile, it also provides an avenue for realizing the value-added utilization of heavy oil in an alternative field.

1. Introduction

With the rapid development of economy and the large consumption of limited fossil fuels, the high-performance and low-cost energy storage devices are urgently needed to promote the practical utilization of renewable energy. Due to the advantages of high energy density and long cycle life, lithium ion batteries (LIBs) have become one of the most promising power sources and have aroused wide public attention in academia and industry[1–3]. In addition, another kind of alkali metal, potassium, has attracted extensive attention due to its similar redox potential to lithium (Li^+/Li = 3.04 V vs SHE, K^+/K = 2.93 V vs SHE) [4,5]. While many materials are difficult to meet the requirements of K^+ intercalation and deintercalation derived from its exaggerated atomic radius (1.38 Å) [6], the search for applicable materials of K-ion storage gradually becomes a significant part of the research of potassium ion batteries.

Recently, carbonaceous electrode materials have been widely studied to promote their practical applications [7–10]. Graphite that is currently commercially available has a low theoretical specific capacity (372 mAh g^{-1}) for lithium storage, which restricts its use in high-power and large-scale energy storage and fails to meet the growing demand [11,12]. In order to improve the situation, it is necessary to develop and design an alternative kind of high-performance carbon material. As a result, various carbon materials including carbon nanotubes [13], graphene [14] and carbon nanofibers and their composite materials [15–17] were studied, especially heteroatom doped carbon materials [18]. Heteroatoms like B, N, P, O or S doped and co-doped into the carbon skeleton can adjust the electronic structure [19–21], and increase the reactivity, as well as modulate the microstructure for enhanced electrochemical performance for Li-ion and K-ion storage [22–24].

Among these heteroatoms, nitrogen is reasonably attractive owing to its relatively higher electronegativity (nitrogen 3.0, carbon 2.5) [25–27], smaller atomic diameter, and additional free electrons that can play an important role in the carbon conductive band. Moreover, the nitrogen doping will also adjust electronic structure and bring more vacancy defects, which generates more active sites between interaction process of alkali metals and nitrogen-rich carbon to improve ion storage performance [28,29]. Especially, the two-dimensional (2D) carbon nanostructures, like nitrogen-doped graphene and carbon nanoflakes, have arouse wide

* Corresponding author.
E-mail address: wumb@upc.edu.cn (M. Wu).

https://doi.org/10.1016/j.carbon.2020.04.034
0008-6223/

attention worldwide due to open structure, adequate interface contract with electrolytes, and rapid electron transport [30–34]. In addition, the dominant capacitance surface drive mechanism revealed by kinetic analysis further emphasizes the enhancement of electron/ionic conductivity by nitrogen doping[35]. Although remarkable progress has been made in nitrogen doped high-performance carbon anodes in recent years, it is still necessary to explore a green and scalable route for preparing nitrogen-doped carbon anodes for pseudocapacitive lithium and potassium storage [36–38].

Therefore, in this paper, a simple and convenient molten salt method was developed to generate ultra-thin nitrogen-doped carbon nanosheets with melamine and asphalt as the nitrogen source and carbon precursor, respectively. It is worth mentioning that the use of KCl-$CaCl_2$ molten salt with a melting point of 600 °C can provide stable and uniform reactive liquid environment. The unique reaction media as well as the deliberately introduced nitrogen source can effectively enhance amorphous degree of asphalt-derived carbon, thus enlarging its interlayer spacing and providing more active sites and defects. The nitrogen doped slim carbon nanosheets (NSCN) were electrochemically tested as anode materials in LIBs and KIBs, and the results showed that it has the expected ultra-high reversible capacity and rate capability, which can be attributed to its unique microstructure. This work provides insights into the role of nitrogen doping in enhancing both ultra-high specific capacity and stability of carbon materials for high-performance lithium and potassium storage.

2. Experimental

2.1. Materials

Petroleum asphalt was obtained from China Petrochemical Corporation (SINOPEC) as a precursor. Melamine ($C_3H_6N_6$, AR), Potassium chloride (KCl, AR) and Calcium chloride ($CaCl_2$, AR) were purchased from MACKLIN.

2.2. General procedure for synthesis of NSCN

Typically, petroleum asphalt (0.5 g), melamine (0.25, 0.5 and 1 g), and the eutectic molten salt (10 g) of KCl/$CaCl_2$ (mass ratio 2:1) were premixed in an agate mortar. The above mixture was ball-milled for 30 min by planetary ball mill at a rotation speed of 800 r min^{-1}, and the uniform brown powder was collected. Then, the mixture was calcinated under N_2 to 800 °C (5 °C min^{-1}) for 2 h. After cooling to ambient temperature, the resultant simples were soaked totally in 1 M HCl solution to remove salts, and then filtered by the deionized water and desiccated under 60 °C for 12 h. The purposed products were labeled as NSCN-x at the mass ratio of melamine to petroleum asphalt (x = 0.5, 1, 2).

To verify the synergistic effect of melamine and molten salts, samples without the molten salts were named as the petroleum asphalt-base nitrogen-doped carbon material (PANC), samples without melamine were named as the molten salt template-obtained carbon material (MSC), and samples without the molten salts and melamine were named as the petroleum asphalt-base carbon material (PAC), respectively.

2.3. Materials characterization

The Hitachi S-4800 was used to present by scanning electron microscopy (SEM) for the morphologies of the carbon samples. The JEM-2010 system was used to measure the Transmission electron microscopy (TEM). The Shimadzu SPM-9700 was used to characterize atomic force microscopy (AFM) for the topographic data. The X'Pert PRO MPD diffractometer using Cu Kα radiation was used to characterize the X-ray diffraction (XRD) and the Renishaw RM2000 (512 nm laser) was used to investigate Raman for the crystallinity. The Micromeritics 3 Flex analyzer was used to measure specific surface area (SSA) and pore properties by the adsorption/desorption of N_2 of the Brunauer-Emmet-Teller (BET) method. The Thermo Scientific ESCALAB 250XI spectrometer (Al Kα radiation) was used to detect X-ray photoelectron spectroscopy (XPS) for chemical composition.

2.4. Electrochemical measurements

In a typical process, active materials, super-P, and polyvinylidene difluoride (PVDF) (8:1:1 wt%) were mixed evenly. Next, the mixture was coated onto Cu foil and desiccated in a vacuum oven at 80 °C for 12 h. The areal loading amount of carbon was 0.9–1.4 mg cm^{-2}. To assemble the Li-ion and K-ion half cells in an argon-filled glovebox, polypropylene film and lithium metal piece were used as the diaphragm and the counter electrode for LIBs, respectively. Similarly, the glass fiber and potassium foil were used for KIBs. The electrolyte was comprised of 1 M $LiPF_6$ and 0.5 M KPF_6 in ethylene carbonate (EC) and dimethyl carbonate (DMC) (1:1 vol %) for LIBs and KIBs. The Land CT2001A battery tester was used to performed the galvanostatic charge/discharge cycles and rate performances in the voltage range of 0.01–3 V. The CHI760D electrochemical workstation was used to measured cyclic voltammetry (CV) and electrochemical impedance spectroscopy (EIS) measurements, which the CV curves were scanned at 0.2 mV s^{-1} between 0.01 and 3 V and the EIS plots were recorded at 0.01 Hz to100 kHz frequency range.

3. Result and discussion

The synthetic process of the nitrogen-doped hierarchical carbon nanosheets is presented in Scheme 1 using a facile, adjustable and cost-effective approach. First, petroleum asphalt, melamine, and mixed salt of KCl and $CaCl_2$ were fully grounded in the planetary ball mill. Subsequently, the mixture was directly pyrolyzed in an inert atmosphere. In this process, the resulting carbon material was laminated due to the role of molten salt and nitrogen atoms from the pyrolysis of melamine were incorporated into the carbon skeleton. After a simple washing step for salt removing, the final product was received. During the process of pyrolysis, the melamine was first condensed into to g-C_3N_4, then the g-C_3N_4 was further pyrolyzed into provide active species for nitrogen doping. As shown in Table S1, the NSCN show a higher carbon yield than that of other products so the carbon in g-C_3N_4 may partially enter the final products. In addition, the molten salt reduces the g-C_3N_4 synthesis temperature and shortens the reaction time. More specifically, g-C_3N_4 can be formed at a temperature as low as 400 °C (as shown in Fig. S1). As a consequence, we believe that this two-dimensional ultra-thin defect-rich carbon nanosheets were produced during the carbonization process due to the synergistic effect of melamine and molten salt.

The SEM and TEM images of the NSCN were displayed in Fig. 1. Compared to the blocky structure of PAC (Fig. S2), the SEM (Fig. 1a–c) and TEM (Fig. 1d–f) images of the NSCN clearly exhibit a unique sheet-like nanostructure with the wave-like morphology and wrinkle. However, there are some differences between them caused by the added amount of melamine. More specifically, NSCN-0.5 shows the interlinked and disordered sheets full of bumps and hollows. With the nitrogen content increasing, both NSCN-1 and NSCN-2 possess the stacking of ultra-thin nanosheet structure, and NSCN-1 shows smooth and light as a crumpled silk (Figs. 1b, 2a-c). By contrast, NSCN-2 displays a thicker sheet-type morphology, and

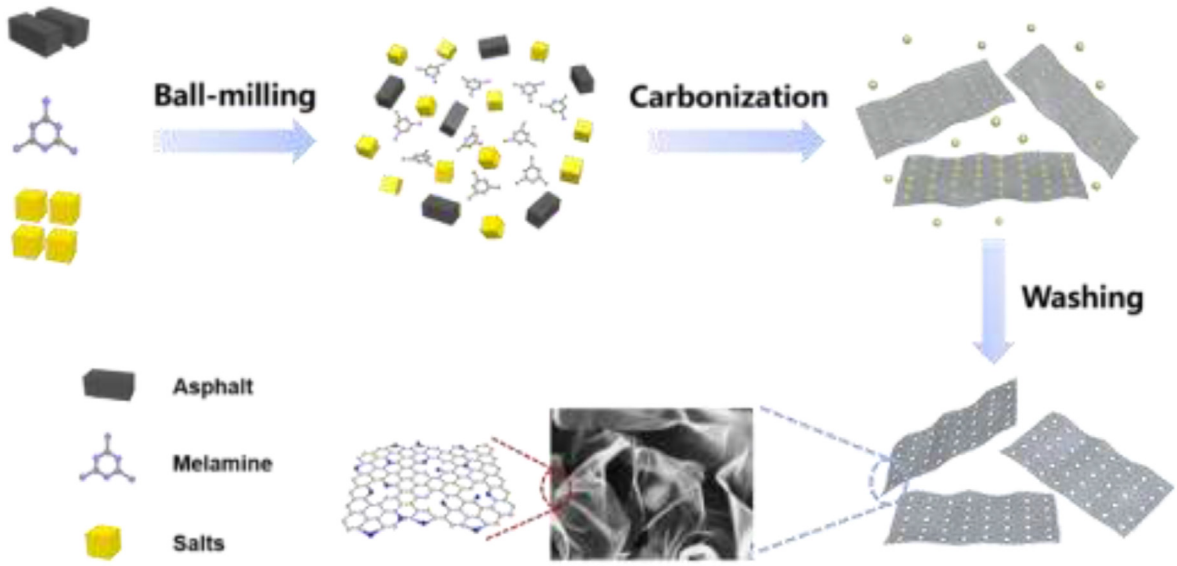

Scheme 1. Illustration of the preparation process of NSCN.

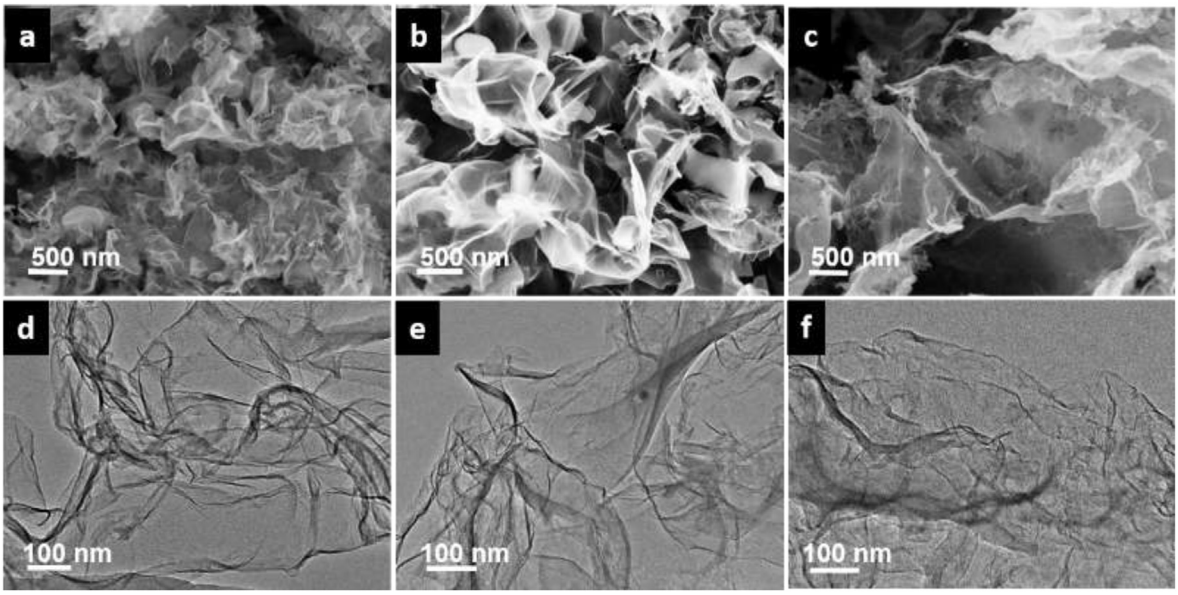

Fig. 1. (a-c) SEM and (d-f) TEM images of NSCN-0.5 (a, d), NSCN-1 (b, e) and NSCN-2 (c, f).

these nanosheets are slightly clustered. Meanwhile, it also offers the microporous structure. This will be verified in subsequent nitrogen adsorption and desorption tests.

Fig. 2a–c reveals the microcosmic appearance of NSCN-1 by the SEM and TEM in detail, there are hierarchical graphene-like lamella folded into various shapes with numerous defects in NSCN-1. In addition, the high-resolution transmission electron microscope (HRTEM) image (Fig. 2d) further indicates the lamellar thickness of NSCN-1 is about 4 nm, which is consistent with the result characterized by AFM of ~3.8 nm (Fig. 2e). The selected area electron diffraction (SAED) pattern (the insert in Fig. 2d) exhibits the (100) and (002) diffraction rings of amorphous nanostructure. Meanwhile, the EDS analyses (Fig. 2f) reveal the existence of C, O and N elements and the even distribution of N element throughout the carbon skeleton.

Futhermore, the elemental composition and relative content of the NSCN are proved by the full scan XPS (Fig. 3a) [39], which shows three peaks centered at binding energies of ca. 284.6 eV, 401.0 eV and 532.0 eV are assigned to C 1s, N 1s and O 1s, respectively [40]. With the addition of melamine content, the peak intensity of nitrogen is increased significantly. The nitrogen content of NSCN is listed in Table S2 which depends on the amount of melamine, and the nitrogen content of NSCN-1 is 3.74 wt%. Moreover, on the basis of chemical state of doped N atoms, the N 1s peak of NSCN-1 could be divided into three main peaks, i.e. in Fig. 3b, including pyridinic N (397.9 eV), pyrrolic N (400.1 eV), and quaternary N (403.8 eV) [41,42]. In detail, the percentage of the nitrogen bonding configurations can be obtained from the integral area and the calculated content of pyrrolic N is 61.1%, much higher than that for pyridinic N (18.8%) and graphitic N (20.1%). The N 1s peaks of NSCN-0.5 and NSCN-2 are shown in Fig. S3. Pyridinic N and pyrrolic N can improve the surface charge distribution of carbon lamella and bring

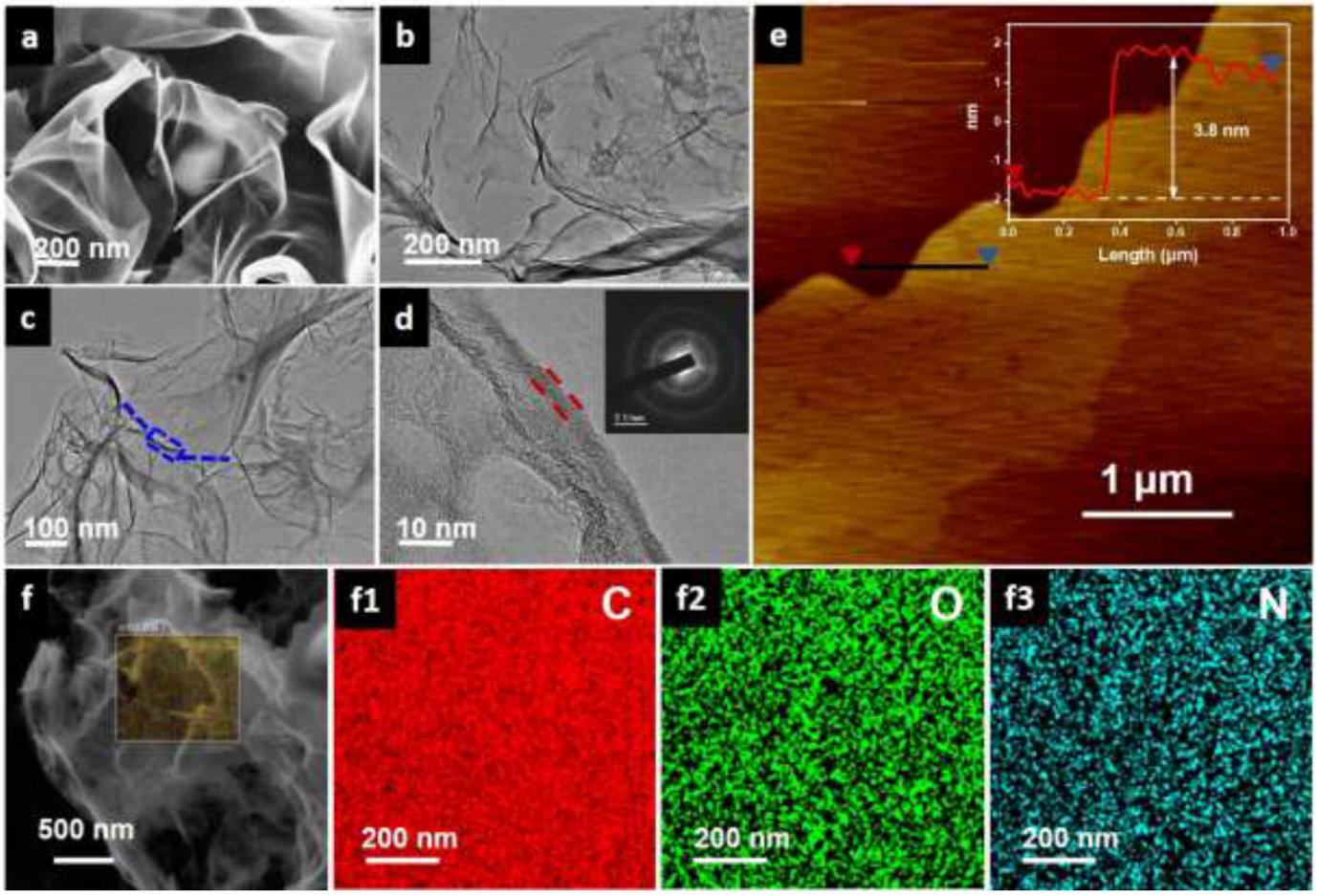

Fig. 2. (a-d) SEM, TEM and HRTEM images of NSCN-1, (e) AFM image of NSCN-1 and inset is the height distribution of the selected area, (f) SEM image of NSCN-1 and the corresponding energy dispersive spectroscopy (EDS) element mapping of (f1) C, (f2) O and (f3) N elements. (A colour version of this figure can be viewed online.)

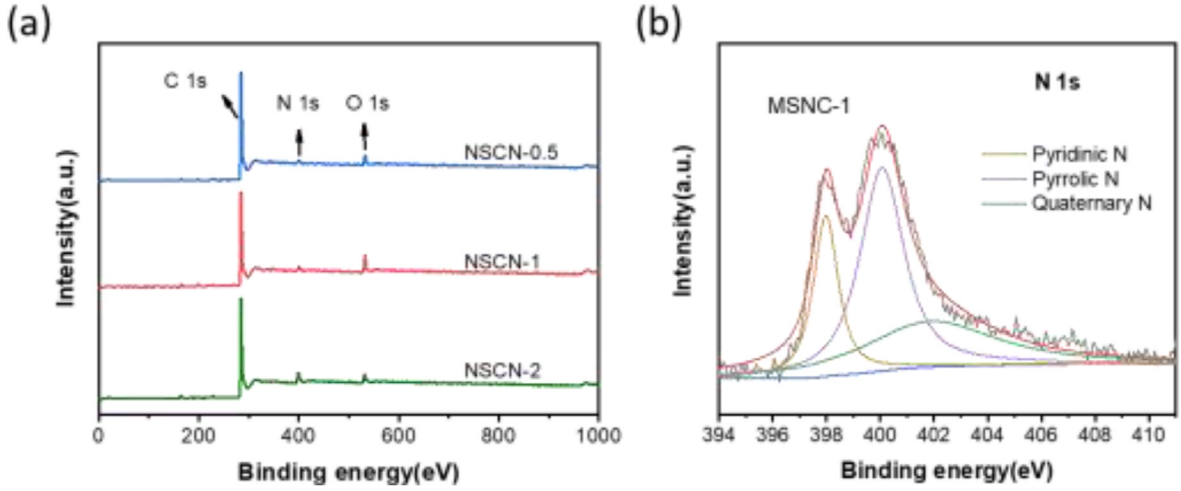

Fig. 3. (a) XPS spectra of the NSCN, (b) high-resolution XPS spectrum of N 1s in the NSCN-1. (A colour version of this figure can be viewed online.)

local electron deficiency, which are reasonably conducive in ion diffusion kinetics and lithium/potassium storage by surface adsorption [43].

The physical microstructures of NSCN are further confirmed by XRD and Raman spectroscopy. Fig. 4a shows a wide diffraction peak at ~25°and a less dramatic peak at ~43° in NSCN, which can correspond to the (002) and (100) planes of graphitic carbon [44,45]. The weak and broad peaks of NSCN reveal a disordered structure. Furthermore, the interplanar spacings (d_{002}) can be calculated by the Bragg's law, of which NSCN-0.5, NSCN-1 and NSCN-2 are 0.364 nm, 0.372 nm and 0.356 nm, respectively. All d_{002} values of NSCN are much larger than that (0.349 nm) of bulk

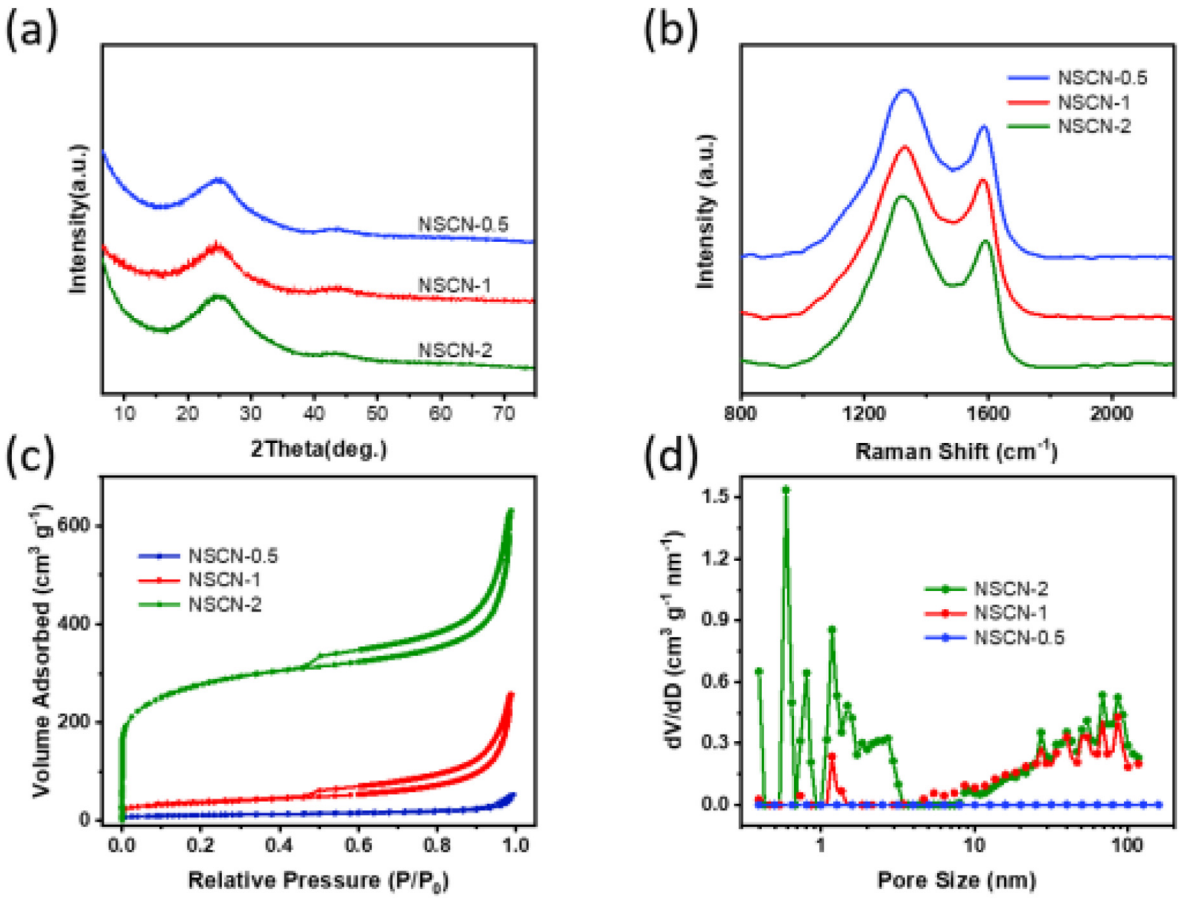

Fig. 4. (a) XRD patterns, (b) Raman spectra, (c) N_2 adsorption and desorption isotherms and (d) pore size distribution of NSCN. (A colour version of this figure can be viewed online.)

petroleum asphalt, accounting that melamine and molten salt have obvious intercalation effect on the graphite layer spacing, which is in favor of the lithium/potassium ion reversible diffusion. G-band around 1590 cm^{-1} and D-band around 1346 cm^{-1} shown in the Raman spectra (Fig. 4b) correspond to the sp^2 carbon and sp^3 carbon [46]. Therefore, the intensity ratio (I_D/I_G) is a credible indicator of the carbon defect and disorder degree. The I_D/I_G values of the NSCN-0.5 (1.26), NSCN-1 (1.21) and NSCN-2 (1.34) are evenly higher than those of MSC (0.87) and PAC (0.81) (Fig. S4), confirming the considerably disordered carbon microstructure of the NSCN. The data elucidates that the enhancement of melamine can substantially increase the defect degree of the material. Additionally, the intensity of the two peaks in NSCN-0.5 and NSCN-2 are stronger than that in NSCN-1, illustrating that NSCN-1 exists a lower degree of disorder. Generally, a appropriate amorphous features favor the insertion/extraction of lithium ions, however, excessive amorphous characteristics weaken the bonding with lithium ions, resulting in lower specific capacity [47]. The data of d_{002} and I_D/I_G of all samples are shown in Table S1.

As stated, nitrogen-doped carbon nanostructure can generate a large amount of defects and vacancies which can elevate the active sites [26]. In order to further characterize the porosity changes of NSCN, N_2 adsorption-desorption analysis was performed. Fig. 4c describes the nitrogen adsorption and desorption isotherms with a type IV features [48]. The SSA and pore volume of NSCN are summarized in Table S1. Furthermore, there is a marked growth trend about the SSA for NSCN-0.5, -1 and -2 (38, 126 and 984 $m^2\ g^{-1}$) originated from nitrogen-doped system, much larger than that of PAC (4 $m^2\ g^{-1}$), confirming that the increase of nitrogen dopants facilitates the formation of porous structure. Such hierarchical porous structure of NSCN-1 with micropores and mesopores can provide abundant active sites and improve the diffusion of Li^+/K^+ [49]. The pore size distribution curves in Fig. 4d demonstrate that there are a large amount of micropores in NSCN-0.5 and NSCN-1 (0.5-2 nm). In addition, more mesopores are emerged in NSCN-2. During the charging/discharging process, Li^+/K^+ preferably residing in the pores rather than on the layers relatively decreases the volume change [50]. Nevertheless, the existence of over-abundant porous structure and excessively large micropore volume (0.98 $cm^3\ g^{-1}$) in NSCN-2 would cause the lengthened ion diffusion path and consume more Li^+/K^+ in the electrolyte during the formation of a stable solid electrolyte interphase (SEI) [51].

The as-made materials were evaluated for lithium storage in a half-cell configuration. The electrochemical performances of these carbons are presented in Fig. 5. Fig. 5a measures the initial three cycles of the NSCN electrode in LIBs. The CV curves exhibit that the reduction peaks around 0.8-1 and 1.5 V at first cycling disappear at subsequent cycles, which is attributed to the formation of SEI film resulting in irreversible capacity loss [21]. The two broad oxidation peaks at ~0.2 and ~1.2 V for all these samples are related to the lithium ion reversible insertion/deintercalation. Furthermore, subsequent CV curves coincide perfectly, indicating a good reversibility of electrodes. However, an irregular anodic peak noted at ~2.3 V in the first anodic scan curves of NSCN-0.5 and NSCN-2 may be related with the Li^+ deintercalation from the interface active sites [52]. In the following cycles, the small peak at ~2.3 V vanishes and almost completely reversible charge and discharge process is established from the second lap. The charge-discharge

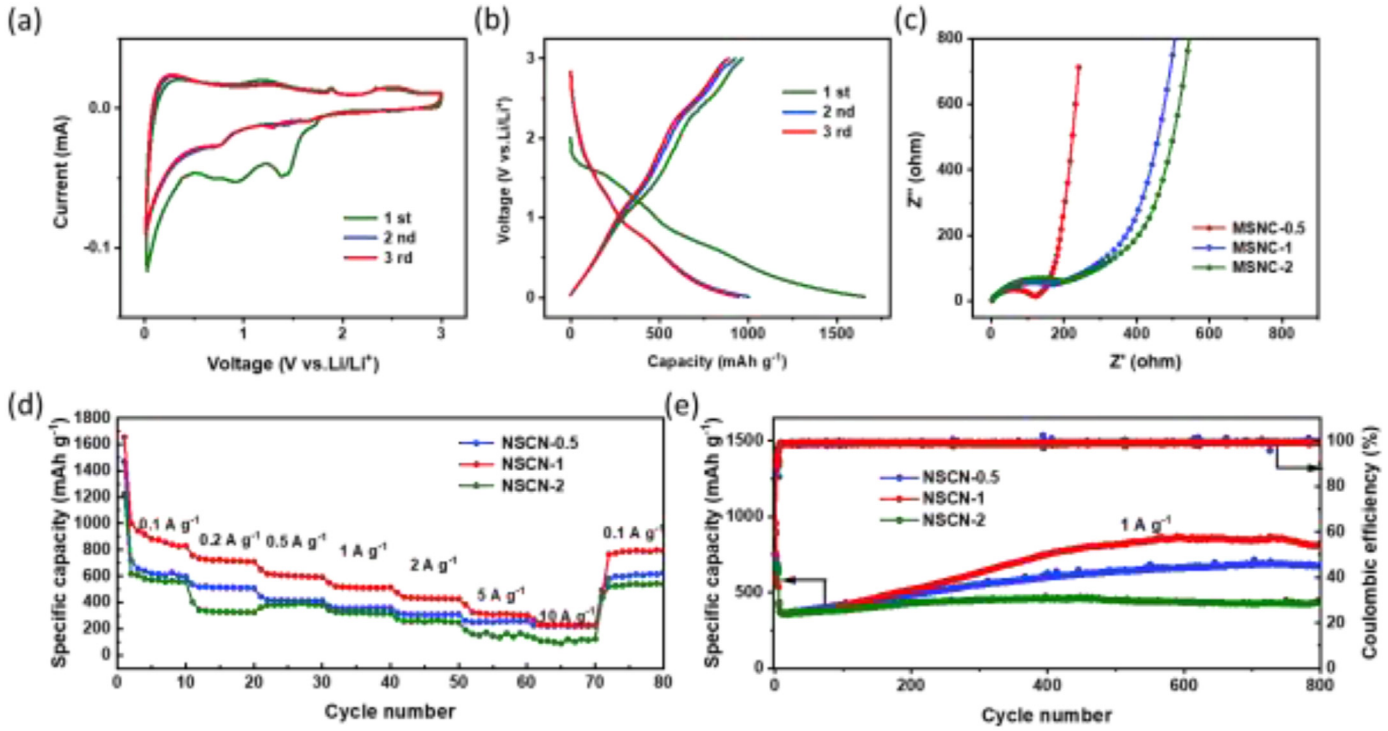

Fig. 5. (a) CV curves, (b) galvanostatic discharge-charge profiles of NSCN-1 at a current density of 100 mA g^{-1}, (c) Nyquist plots, (d)rate performance and (e) cycling performance at a current density of 1 A g^{-1} of NSCN. (A colour version of this figure can be viewed online.)

profiles of NSCN are as shown in Fig. S5b, d and Fig. 5b, the as-obtained NSCN-1 delivers an initial discharge and charge specific capacity of 1653 and 964 mAh g^{-1}, indicating the highest initial Coulombic efficiency (ICE) of 58% among the samples, followed by NSCN-0.5 (48%) and NSCN-2 (50%). Although relatively low ICE and large irreversible capacity are common phenomena for carbon-based materials due to the existence of SEI film, the fact that NSCN-1 shows a higher ICE may be due to that the unique structure of N functionalities acting on nanosheet restrict the formation of the SEI film (as shown Table S3) [53].

EIS measurements between the frequency of 100 kHz and 0.01 Hz are conducted to demonstrate enhancement of the electrode conductivity. As shown in Fig. 5c, the smaller semicircle reflects higher conductivity of NSCN-1 on account of a lower charge transfer resistance compared to NSCN-0.5 and NSCN-2, indicating a faster Li-ion insertion kinetics. Moreover, the steeper long tail of low frequency is related to the lower resistance of the SEI film. The result further signifies that the 2D carbon nanosheets with disordered structure and high SSA are beneficial to lithium-ion insertion or extraction and the charge transfer reaction.

Furthermore, the NSCN exhibit excellent rate performances. As shown in Fig. 5d, electrochemical cycling performances of NSCN at various current densities (0.1-10 A g^{-1}) were investigated. The NSCN-1 anode also delivers the highest specific capacity among the as-prepared samples with 807, 702, 593, 507, 405, 306, and 231 mAh g^{-1} at current densities of 0.1, 0.2, 0.5, 1, 2, 5, and 10 A g^{-1}, respectively. However, NSCN-1 has higher capacity decay rate than NSCN-0.5 at high current densities. It may be due to that the larger SSA causes a faster electrode chemical reaction speed and a lower active material utilization rate [24]. Moreover, the capacity returns to 780 mAh g^{-1} after the current density drops to 0.1 A g^{-1}, giving a high capacity retention (96.8%). Fig. 5e displays the cycling stability of NSCN-1, which exhibits excellent specific capacity of 848 mAh g^{-1} after 800 cycles at 1 A g^{-1}. By contrast, PAC, MSC (Fig. S6), NSCN-0.5 and NSCN-2 retain lower specific capacities of 237, 631, 687 and 442 mAh g^{-1} after 800 cycles at 1 A g^{-1}, indicating that the reasonable degree of nitrogen doping can effectively increase electrochemical performance. A remarkable characteristic of the NSCN electrodes occur that the capacities gradually increase with further cycling. And this phenomenon is much common for carbon material anodes, which may be due to that the excellent nanostructure with relatively large SSA and reasonable porosity is highly accessible for lithium ions to thus provide extra Li^+ storage capacity [54–56]. Such an excellent cyclability of heteroatom-doped carbon anodes is superior to many previously reported carbonaceous electrodes (Table S3), and the overall results well demonstrate that the choreographed nitrogen-doped ultrathin carbon nanosheets have extraordinary potential with enhanced lithium storage.

Furthermore, the electrochemical performance of NSCN-1 as the anodes of KIBs is tested. Fig. 6a shows the CV curves of first three cycles at 0.2 mV s^{-1}. Apparently, two small peaks were observed at 0.5 and 2.3 V during the first cycle, which correspond to K^+ intercalation/deintercalation position [57]. Moreover, a strong redox peak occurs on 0.5-0.7 V, which is principally attributed to the formation of SEI film and the reactions of surface functional groups with potassium, and this peak disappears in the following cycling [58]. Similar to LIBs, NSCN-1 reveals a relatively stable SEI film and favourable cycle performance for KIBs. Fig. 6b shows the voltage/capacity curves of NSCN-1 electrode for initial three cycles at 0.1 A g^{-1}. NSCN-1 delivers a higher inital discharge specific capacity (2158 mAh g^{-1}) but unsatisfied initial Coulomb efficiency (16.7%), which due to the intercalation reaction of K^+ during the first charge/discharge process [59]. Besides, a gentle slope appears around 1 V but disappears in the subsequent loop. As indicated, the irreversible decomposition of the electrolyte is gradually alleviated and inhibited, which is essential to ensure subsequent stable cycling [60]. In addition, the long cycling performances of NSCN-1 is shown in Fig. 6c. As described above, NSCN-1 has quite good

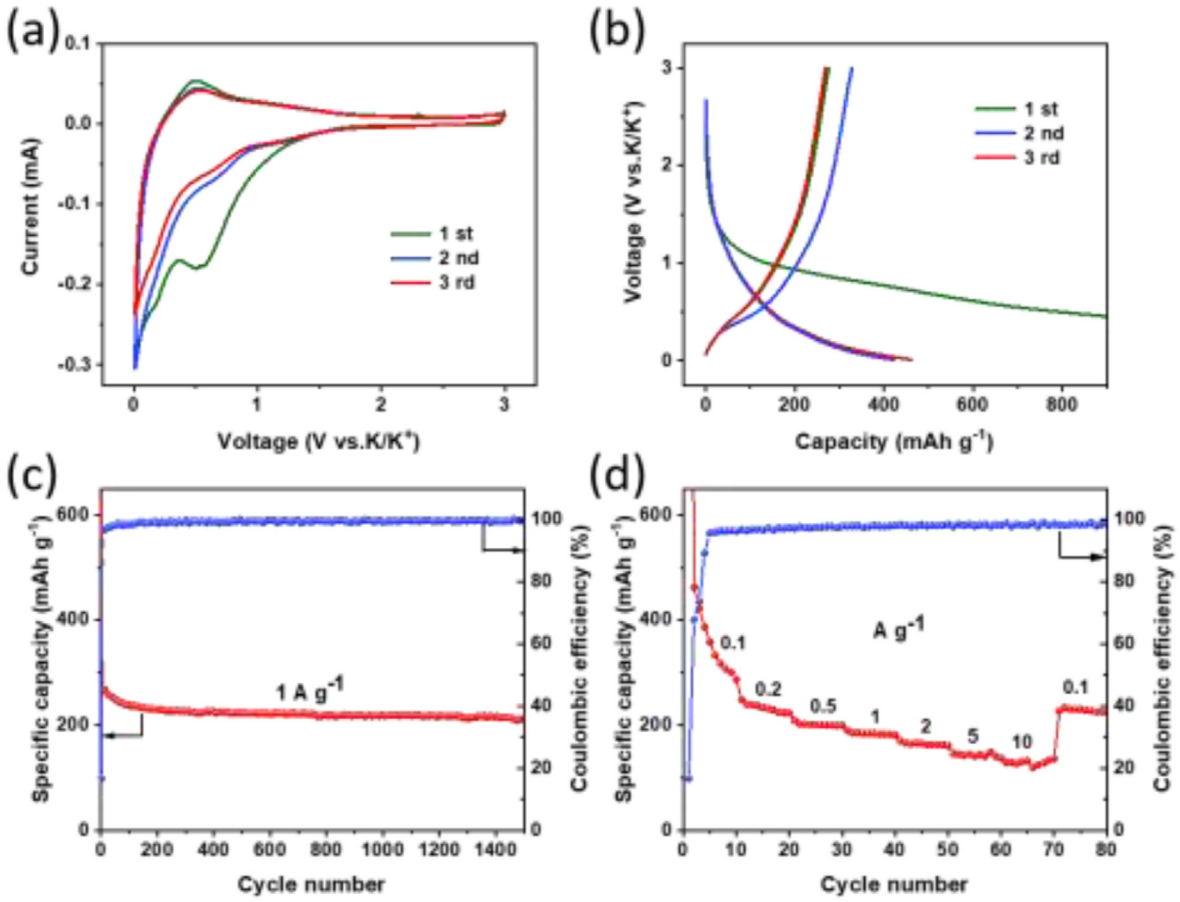

Fig. 6. (a) CV curves and (b) galvanostatic discharge-charge profiles at a current density of 100 mA g^{-1};,(c) cycling performance at a current density of 1 A g^{-1} and (d) rate performance of NSCN-1. (A colour version of this figure can be viewed online.)

retention rate at high current densities, even the discharge specific capacity keeps 214 mAh g^{-1} at 1 A g^{-1} after 1500 cycles, indicating NSCN-1 anode achieves reasonably excellent cycling stability for KIBs. Fig. 6d demonstrates that the rate capacity of NSCN-1 at the different current densities, the electrode obtains the reversible capacities of 318, 232, 201, 185, 165, 144 and 128 mAh g^{-1} at 0.1, 0.2, 0.5, 1, 2, 5 and 10 A g^{-1}, respectively. Beyond that, the capacity returns to 231 mAh g^{-1} after the current density drops to 0.1 A g^{-1}. Therefore, NSCN-1 exhibits enormous potential as the anode of high-performance KIBs.

To further investigate the charge storage mechanism for the NSCN-1 electrodes, CV measurements were conducted at unequal sweep rates from 0.2 mV s^{-1} to 2.0 mV s^{-1} in LIBs (Fig. 7a) and KIBs (Fig. 7e). It is a remarkable fact that the peak current (i) at a specified potential is not proportional to the square root of the scan rate (v), revealing that the redox process of the electrodes is not merely the ion-diffusion control process [61,62]. Generally, the corresponding peak current varies with the sweep rate following the equation:

$$i\,(v) = av^b \tag{1}$$

$$\log i\,(v) = \log a + b\log v \tag{2}$$

According to reported researches, the parameter b can be obtained by means of linearly fitted from log (i) versus log (v), which determines whether existence of pseudocapacitive behavior during the during charge and discharge cycles [63,64]. A b value of 0.5 means that the electrode materials behave as battery property; while the b value is greater than or equal to 1, illustrating that $i\,(v) = av$ and the response peak current varies linearly with the scan rate, which represents the ideal capacitive behaviour [65]. As shown in Fig. 7b and f by drawing the appropriate lines of log (i) and log (v) at varies potentials of the reduction process, a range of b values corresponding to different voltages larger than 0.75 are obtained for Li/K storage, confirming an evident pseudocapacitive contribution for the NSCN-1 electrode. Moreover, charge storage contribution rate can be calculated via Dunn's method as follows:

$$i\,(V) = i_{\mathrm{cap}} + i_{\mathrm{diff}} = k_1\,v + k_2\,v^{1/2} \tag{3}$$

By rearranging eq (3) to:

$$i\,(V)/\,v^{1/2} = k_1\,v^{1/2} + k_2 \tag{4}$$

the k_1 and k_2 values can be determined from fitting the linear of $i(V)/v^{1/2}$ and $v^{1/2}$ easily. In consequence, the capacitive current can be calculated through the formula of $i_{\mathrm{cap}}(V) = k_1 v$, which could obtain the percentage in total current. As shown in Fig. 7c and g, it is discovered that approximately 78% capacity in LIBs and 74% capacity in KIBs derive from pseudocapacitance contribution at a scan rate of 1 mV s^{-1} for the NSCN-1. Moreover, the pseudocapacitive contribution was indicated to be related to scan rate and raises with increased sweep rates in both LIBs and in KIBs (Fig. 7d and h). The obvious pseudocapacitive behavior is generally due to the large SSA caused by ultra-thin nanostructure which facilitates the adsorption

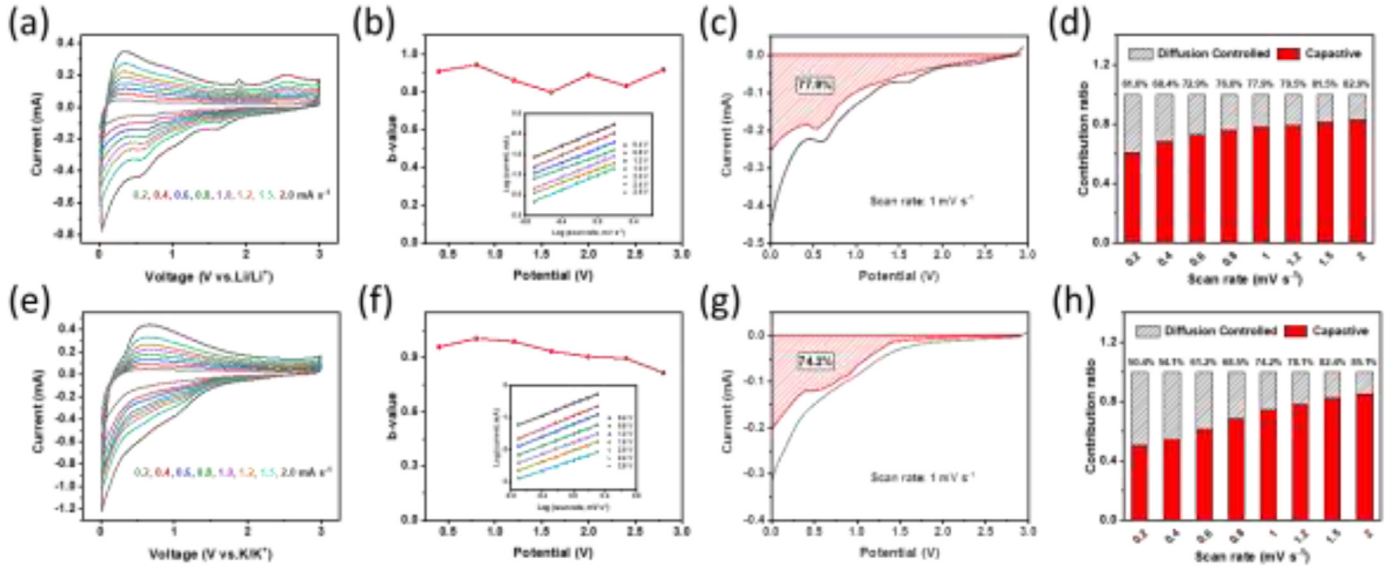

Fig. 7. CV curves of NSCN-1 at different scan rates in (a) LIBs and (e) KIBs; *b* values plotted against battery potential of NSCN-1 for cathodic scans in (b) LIBs and (f) KIBs. The insets are the current responses plotted against scan rates of NSCN-1 at various potentials; Capacitive contribution to the reduction process at the scan rates of 1 mV s^{-1} marked by the shaded region in (c) LIBs and (g) KIBs; Percentage of capacitive contributions at different scan rates for the NSCN-1 electrode in (d) LIBs and (h) KIBs. (A colour version of this figure can be viewed online.)

of more charge on the carbon surface.

According to the aforementioned discussions, the excellent electrochemical performances of the choreographed ultrathin carbon nanosheets, including the outstanding cycling stability, large specific capacity and rate capability, can be attributed to the combined effects of the following factors. Firstly, the ultrathin 2D carbon nanosheets possess large interlayer space, expose abundant active sites and provide short ionic diffusion path, which are conductive to the insertion and extraction of ions [24,66]. Secondly, the outer nitrogen-riched nanostructures play a key role in enhancing the substantial defects and exposing large quantities of active sites. The reason is that the highly wrinkle surface could prevent the restacking of these nanosheets when aggregated into electrode architecture [67,68], which will permit the active sites to be effective in practical applications. In addition, the charge is more likely to gather around vacancy defects in NSCN, thereby improving Li^+ and K^+ adsorption capacity and increasing electronic conductivity [69]. Moreover, the pseudocapacitance effect also contributes significantly to the improvement of the extra Li^+/K^+ storage as previously mentioned.

4. Conclusions

In summary, we demonstrated a facile molten-salt-mediated production of ultrathin carbon nanosheets with tunable nitrogen doping using low-cost precursors including asphalt and melamine. In this process, melamine was used as both nitrogen source and *in-situ* template, which would react with the molten salt and simultaneously generate the ultrathin 2D amorphous carbon nanosheets during carbonization. The N-doped 2D carbon structure with increased interlayer distance, high disordered degree and effective active surface results in significant improvement for Li^+/K^+ storage and migration. When applied as negative electrodes for LIBs and KIBs, NSCN-1 offers superior rate capability and ultra-long cycling life and high specific reversible capacity of 848 mAh g^{-1} after 800 cycles and 214 mAh g^{-1} after 1500 cycles at 1 A g^{-1}, respectively. Moreover, this work not only provides a universal and well-designed route for the synthesis of hierarchical carbon nanosheets, but also achieves the construction of the pseudocapacitive-capable Li^+/K^+ anodes with outstanding specific capability, rate capability and cycling stability.

Declaration of competing interest

The authors declare that they have no known competing financial interests or personal relationships that could have appeared to influence the work reported in this paper.

CRediT authorship contribution statement

Tingyue Peng: Conceptualization, Methodology, Software, Data curation, Visualization, Investigation, Writing - original draft. **Zhonghao Tan:** Visualization, Supervision, Writing - review & editing. **Mengdi Zhang:** Visualization, Supervision, Writing - review & editing. **Linqing Li:** Visualization, Supervision, Writing - review & editing. **Yixian Wang:** Visualization, Writing - review & editing. **Lu Guan:** Supervision, Software. **Xiaojie Tan:** Methodology, Software. **Lei Pan:** Methodology, Supervision. **Haiqiu Fang:** Supervision, Conceptualization. **Mingbo Wu:** Project administration, Investigation, Writing - review & editing.

Acknowledgements

This work is financially supported by Scientific Research and Technology Development Project of Petrochina Co., LTD (2016B-2004(GF)), the Fundamental Research Funds for the Central Universities (15 C × 08005 A), the Financial Support from Tai Shan Scholar Project (No.ts201712020), Technological Leading Scholar of 10000 Talent Project (No. W03020508), Shandong Provincial Natural Science Foundation (ZR2018ZC1458).

Appendix A. Supplementary data

Supplementary data to this article can be found online at https://doi.org/10.1016/j.carbon.2020.04.034.

References

[1] J. Meng, H. Guo, C. Niu, Y. Zhao, L. Xu, Q. Li, et al., Advances in structure and property optimizations of battery electrode materials, Joule 1 (3) (2017) 522–547.

[2] H. Li, Z. Wang, L. Chen, X. Huang, Research on advanced materials for Li-ion batteries, Adv. Mater. 21 (45) (2009) 4593–4607.

[3] D. Di Lecce, R. Verrelli, J. Hassoun, Lithium-ion batteries for sustainable energy storage: recent advances towards new cell configurations, Green Chem. 19 (15) (2017) 3442–3467.

[4] Z. Ju, S. Zhang, Z. Xing, Q. Zhuang, Y. Qiang, Y. Qian, Direct synthesis of few-layer F-doped graphene foam and its lithium/potassium storage properties, ACS Appl. Mater. Interfaces 8 (32) (2016) 20682–20690.

[5] Z. Jian, W. Luo, X. Ji, Carbon electrodes for K-ion batteries, J. Am. Chem. Soc. 137 (36) (2015) 11566–11569.

[6] Q. Sun, D. Li, J. Cheng, L. Dai, J. Guo, Z. Liang, et al., Nitrogen-doped carbon derived from pre-oxidized pitch for surface dominated potassium-ion storage, Carbon 155 (2019) 601–610.

[7] J. Lu, Z. Chen, Z. Ma, F. Pan, L.A. Curtiss, K. Amine, The role of nanotechnology in the development of battery materials for electric vehicles, Nat. Nanotechnol. 11 (2016) 1031.

[8] X. Jiang, W. Yu, H. Wang, H. Xu, X. Liu, Y. Ding, Enhancing the performance of MnO by double carbon modification for advanced lithium-ion battery anodes, J. Mater. Chem. 4 (3) (2016) 920–925.

[9] S.K. Park, J. Lee, S. Bong, B. Jang, K.D. Seong, Y. Piao, Scalable synthesis of few-layer MoS_2 incorporated into hierarchical porous carbon nanosheets for high-performance Li- and Na-ion battery anodes, ACS Appl. Mater. Interfaces 8 (30) (2016) 19456–19465.

[10] L. Wang, J. Han, D. Kong, Y. Tao, Q.-H. Yang, Enhanced roles of carbon architectures in high-performance lithium-ion batteries, Nano-Micro Lett. 11 (1) (2019) 5.

[11] F. Bonaccorso, L. Colombo, G. Yu, M. Stoller, V. Tozzini, A.C. Ferrari, et al., 2D materials. Graphene, related two-dimensional crystals, and hybrid systems for energy conversion and storage, Science 347 (6217) (2015) 1246501.

[12] X.Y. Zhang, L.L. Hou, A. Ciesielski, P. Samori, 2D materials beyond graphene for high-performance energy storage applications, Adv. Energy Mater. 6 (23) (2016) 21.

[13] Q. Li, J. Wu, J. Xu, V.P. Dravid, Synergistic sodiation of cobalt oxide nanoparticles and conductive carbon nanotubes (CNTs) for sodium-ion batteries, J. Mater. Chem. 4 (22) (2016) 8669–8675.

[14] J. Niu, J. Liang, R. Shao, M. Liu, M. Dou, Z. Li, et al., Tremella-like N, O-codoped hierarchically porous carbon nanosheets as high-performance anode materials for high energy and ultrafast Na-ion capacitors, Nano Energy 41 (2017) 285–292.

[15] B. Wang, T. Qiu, X. Li, B. Luo, L. Hao, Y. Zhang, et al., Synergistically engineered self-standing silicon/carbon composite arrays as high performance lithium battery anodes, J. Mater. Chem. 3 (2) (2015) 494–498.

[16] Y. Tang, Z. Zhao, X. Hao, Y. Wei, H. Zhang, Y. Dong, et al., Cellular carbon-wrapped $FeSe_2$ nanocavities with ultrathin walls and multiple rooms for ion diffusion-confined ultrafast sodium storage, J. Mater. Chem. 7 (9) (2019) 4469–4479.

[17] X. Wang, Y. Chen, Y. Fang, J. Zhang, S. Gao, X.W. Lou, Synthesis of cobalt sulfide multi-shelled nanoboxes with precisely controlled two to five shells for sodium-ion batteries, Angew. Chem. Int. Ed. 58 (9) (2019) 2675–2679.

[18] W. Shao, F. Hu, C. Song, J. Wang, C. Liu, Z. Weng, et al., Hierarchical N/S co-doped carbon anodes fabricated through a facile ionothermal polymerization for high-performance sodium ion batteries, J. Mater. Chem. 7 (11) (2019) 6363–6373.

[19] Q. Feng, H. Li, Z. Tan, Z. Huang, L. Jiang, H. Zhou, et al., Design and preparation of three-dimensional MnO/N-doped carbon nanocomposites based on waste biomass for high storage and ultra-fast transfer of lithium ions, J. Mater. Chem. 6 (40) (2018) 19479–19487.

[20] C. Gao, J. Feng, J. Dai, Y. Pan, Y. Zhu, W. Wang, et al., Manipulation of interlayer spacing and surface charge of carbon nanosheets for robust lithium/sodium storage, Carbon 153 (2019) 372–380.

[21] D. Zheng, J. Zhang, W. Lv, T. Cao, S. Zhang, D. Qiu, et al., Sulfur-functionalized three-dimensional graphene monoliths as high-performance anodes for ultrafast sodium-ion storage, Chem. Commun. 54 (34) (2018) 4317–4320.

[22] G. Zou, H. Hou, C.W. Foster, C.E. Banks, T. Guo, Y. Jiang, et al., Advanced hierarchical vesicular carbon Co-doped with S, P, N for high-rate Sodium Storage, Adv. Sci. 5 (7) (2018) 1800241.

[23] X. Wu, Y. Chen, Z. Xing, C.W.K. Lam, S.-S. Pang, W. Zhang, et al., Advanced carbon-based anodes for potassium-ion batteries, Adv. Energy Mater. 9 (21) (2019) 1900343.

[24] X. Zheng, J. Luo, W. Lv, D.-W. Wang, Q.-H. Yang, Two-dimensional porous carbon: synthesis and ion-transport properties, Adv. Mater. 27 (36) (2015) 5388–5395.

[25] J. Chen, Z. Mao, L. Zhang, D. Wang, R. Xu, L. Bie, et al., Nitrogen-deficient graphitic carbon nitride with enhanced performance for lithium ion battery anodes, ACS Nano 11 (12) (2017) 12650–12657.

[26] J. Chen, Z. Mao, L. Zhang, Y. Tang, D. Wang, L. Bie, et al., Direct production of nitrogen-doped porous carbon from urea via magnesiothermic reduction, Carbon 130 (2018) 41–47.

[27] Z. Yu, X. Wang, Y.-N. Hou, X. Pan, Z. Zhao, J. Qiu, Nitrogen-doped mesoporous carbon nanosheets derived from metal-organic frameworks in a molten salt medium for efficient desulfurization, Carbon 117 (2017) 376–382.

[28] J. Chen, J. Xu, S. Zhou, N. Zhao, C.-P. Wong, Nitrogen-doped hierarchically porous carbon foam: a free-standing electrode and mechanical support for high-performance supercapacitors, Nano Energy 25 (2016) 193–202.

[29] X. Zheng, W. Lv, Y. Tao, J. Shao, C. Zhang, D. Liu, et al., Oriented and interlinked porous carbon nanosheets with an extraordinary capacitive performance, Chem. Mater. 26 (23) (2014) 6896–6903.

[30] Y. Fang, Y. Lv, R. Che, H. Wu, X. Zhang, D. Gu, et al., Two-dimensional mesoporous carbon nanosheets and their derived graphene nanosheets: synthesis and efficient lithium ion storage, J. Am. Chem. Soc. 135 (4) (2013) 1524–1530.

[31] X. Liu, C. Giordano, M. Antonietti, A facile molten-salt route to graphene synthesis, Small 10 (1) (2014) 193–200.

[32] T. Shang, Y. Xu, P. Li, J. Han, Z. Wu, Y. Tao, et al., A bio-derived sheet-like porous carbon with thin-layer pore walls for ultrahigh-power supercapacitors, Nano Energy 70 (2020) 104531.

[33] Q. Liang, L. Ye, Z.H. Huang, Q. Xu, Y. Bai, F. Kang, et al., A honeycomb-like porous carbon derived from pomelo peel for use in high-performance supercapacitors, Nanoscale 6 (22) (2014) 13831–13837.

[34] H. Hu, M. Wu, Heavy oil-derived carbon for energy storage applications, J. Mater. Chem. 8 (15) (2020) 7066–7082.

[35] P. Li, J.-Y. Hwang, S.-M. Park, Y.-K. Sun, Superior lithium/potassium storage capability of nitrogen-rich porous carbon nanosheets derived from petroleum coke, J. Mater. Chem. 6 (26) (2018) 12551–12558.

[36] X. Liu, M. Antonietti, Moderating black powder chemistry for the synthesis of doped and highly porous graphene nanoplatelets and their use in electrocatalysis, Adv. Mater. 25 (43) (2013) 6284–6290.

[37] X. Liu, N. Fechler, M. Antonietti, Salt melt synthesis of ceramics, semiconductors and carbon nanostructures, Chem. Soc. Rev. 42 (21) (2013) 8237–8265.

[38] Y. Wang, Y. Wang, J. Liu, L. Pan, W. Tian, M. Wu, et al., Preparation of carbon nanosheets from petroleum asphalt via recyclable molten-salt method for superior lithium and sodium storage, Carbon 122 (2017) 344–351.

[39] X. Han, H. Jiang, Y. Zhou, W. Hong, Y. Zhou, P. Gao, et al., A high performance nitrogen-doped porous activated carbon for supercapacitor derived from pueraria, J. Alloys Compd. 744 (2018) 544–551.

[40] X. Wang, Q. Weng, X. Liu, X. Wang, D.M. Tang, W. Tian, et al., Atomistic origins of high rate capability and capacity of N-doped graphene for lithium storage, Nano Lett. 14 (3) (2014) 1164–1171.

[41] B. He, W.-C. Li, A.-H. Lu, High nitrogen-content carbon nanosheets formed using the Schiff-base reaction in a molten salt medium as efficient anode materials for lithium-ion batteries, J. Mater. Chem. 3 (2) (2015) 579–585.

[42] X. Hao, J. Wang, B. Ding, L. Shen, Y. Xu, Y. Wang, et al., Heteroatom-doped porous carbon nanosheets: general preparation and enhanced capacitive properties, Chemistry 22 (46) (2016) 16668–16674.

[43] J. Jin, Z. Wang, R. Wang, J. Wang, Z. Huang, Y. Ma, et al., Achieving high volumetric lithium storage capacity in compact carbon materials with controllable nitrogen doping, Adv. Funct. Mater. 29 (12) (2019).

[44] Y. Chen, L. Shi, S. Guo, Q. Yuan, X. Chen, J. Zhou, et al., A general strategy towards carbon nanosheets from triblock polymers as high-rate anode materials for lithium and sodium ion batteries, J. Mater. Chem. 5 (37) (2017) 19866–19874.

[45] J. Dai, J. Liao, M. He, M. Yang, K. Wu, W. Yao, Si@SnS_2–reduced graphene oxide composite anodes for high-capacity lithium-ion batteries, ChemSusChem 12 (23) (2019) 5092–5098.

[46] Y. Zhang, Q. Ma, S. Wang, X. Liu, L. Li, Poly(vinyl alcohol)-Assisted fabrication of hollow carbon spheres/reduced graphene oxide nanocomposites for high-performance lithium-ion battery anodes, ACS Nano 12 (5) (2018) 4824–4834.

[47] Y. Chen, L. Shi, Q. Yuan, A. Li, S. Huang, H.Y. Yang, et al., Crystallization-induced morphological tuning toward denim-like graphene nanosheets in a KCl-copolymer solution, ACS Nano 12 (4) (2018) 4019–4024.

[48] G. Zeng, B. Zhou, L. Yi, H. Li, X. Hu, Y. Li, Green and facile fabrication of hierarchical N-doped porous carbon from water hyacinths for high performance lithium/sodium ion batteries, Sustainable Energy & Fuels 2 (4) (2018) 855–861.

[49] N. Xiao, X. Zhang, C. Liu, Y. Wang, H. Li, J. Qiu, Coal-based carbon anodes for high-performance potassium-ion batteries, Carbon 147 (2019) 574–581.

[50] M. Seredych, D. Hulicova-Jurcakova, G.Q. Lu, T.J. Bandosz, Surface functional groups of carbons and the effects of their chemical character, density and accessibility to ions on electrochemical performance, Carbon 4 6 (11) (2008) 1475–1488.

[51] Y. Wang, W. Tian, L. Wang, H. Zhang, J. Liu, T. Peng, et al., A tunable molten-salt route for scalable synthesis of ultrathin amorphous carbon nanosheets as high-performance anode materials for lithium-ion batteries, ACS Appl. Mater. Interfaces 10 (6) (2018) 5577–5585.

[52] B. Jin, F. Gao, Y.F. Zhu, X.Y. Lang, G.F. Han, W. Gao, et al., Facile synthesis of non-graphitizable polypyrrole-derived carbon/carbon nanotubes for lithium-ion batteries, Sci. Rep. 6 (2016) 19317.

[53] L. Chen, W. Yang, X. Li, L. Han, M. Wei, Co_9S_8 embedded into N/S doped carbon composites: in situ derivation from a sulfonate-based metal-organic framework and its electrochemical properties, J. Mater. Chem. 7 (17) (2019) 10331–10337.

[54] J. Wu, J. Liu, Z. Wang, X. Gong, M. Qi, Y. Wang, N-Doped gel-structures for construction of long cycling Si anodes at high current densities for high performance lithium-ion batteries, J. Mater. Chem. 7 (18) (2019)

11347–11354.
[55] Y. Yan, Y.X. Yin, S. Xin, Y.G. Guo, L.J. Wan, Ionothermal synthesis of sulfur-doped porous carbons hybridized with graphene as superior anode materials for lithium-ion batteries, Chem. Commun. 48 (86) (2012) 10663–10665.
[56] Y. Mao, H. Duan, B. Xu, L. Zhang, Y. Hu, C. Zhao, et al., Lithium storage in nitrogen-rich mesoporous carbon materials, Energy Environ. Sci. 5 (7) (2012) 7950–7955.
[57] J. Yang, Z. Ju, Y. Jiang, Z. Xing, B. Xi, J. Feng, et al., Enhanced capacity and rate capability of nitrogen/oxygen dual-doped hard carbon in capacitive potassium-ion storage, Adv. Mater. 30 (4) (2018) 1700104.
[58] Q. Zhang, J. Mao, W.K. Pang, T. Zheng, V. Sencadas, Y. Chen, et al., Boosting the potassium storage performance of alloy-based anode materials via electrolyte salt chemistry, Adv. Energy Mater. 8 (15) (2018) 1703288.
[59] A. Eftekhari, Z. Jian, X. Ji, Potassium secondary batteries, ACS Appl. Mater. Interfaces 9 (5) (2017) 4404–4419.
[60] J. Bai, B. Xi, H. Mao, Y. Lin, X. Ma, J. Feng, et al., One-step construction of N, P-codoped porous carbon sheets/CoP hybrids with enhanced lithium and potassium storage, Adv. Mater. 30 (35) (2018) 1802310.
[61] D. Li, L. Zhang, H. Chen, J. Wang, L.-X. Ding, S. Wang, et al., Graphene-based nitrogen-doped carbon sandwich nanosheets: a new capacitive process controlled anode material for high-performance sodium-ion batteries, J. Mater. Chem. 4 (22) (2016) 8630–8635.
[62] W. Tian, H. Hu, Y. Wang, P. Li, J. Liu, J. Liu, et al., Metal-organic frameworks mediated synthesis of one-dimensional molybdenum-based/carbon composites for enhanced lithium storage, ACS Nano 12 (2) (2018) 1990–2000.
[63] J. Liu, J. Wang, C. Xu, H. Jiang, C. Li, L. Zhang, et al., Advanced energy storage devices: basic principles, analytical methods, and rational materials design, Adv. Sci. 5 (1) (2018) 1700322.
[64] C-q Yi, J-p Zou, H-z Yang, X. Leng, Recent advances in pseudocapacitor electrode materials: transition metal oxides and nitrides, Trans. Nonferrous Metals Soc. China 28 (10) (2018) 1980–2001.
[65] V. Augustyn, J. Come, M.A. Lowe, J.W. Kim, P.L. Taberna, S.H. Tolbert, et al., High-rate electrochemical energy storage through Li^+ intercalation pseudocapacitance, Nat. Mater. 12 (6) (2013) 518–522.
[66] Z. Li, W. Lv, C. Zhang, B. Li, F. Kang, Q.-H. Yang, A sheet-like porous carbon for high-rate supercapacitors produced by the carbonization of an eggplant, Carbon 92 (2015) 11–14.
[67] K. Share, A.P. Cohn, R. Carter, B. Rogers, C.L. Pint, Role of nitrogen-doped graphene for improved high-capacity potassium ion battery anodes, ACS Nano 10 (10) (2016) 9738–9744.
[68] D. Luo, J. Xu, Q. Guo, L. Fang, X. Zhu, Q. Xia, et al., Surface-dominated sodium storage towards high capacity and ultrastable anode material for sodium-ion batteries, Adv. Funct. Mater. 28 (47) (2018) 1805371.
[69] R. Guo, C. Lv, W. Xu, J. Sun, Y. Zhu, X. Yang, et al., Effect of intrinsic defects of carbon materials on the sodium storage performance, Adv. Energy Mater. 10 (9) (2020) 1903652.